This is a repository copy of *ω phase strengthened 1.2GPa metastable β titanium alloy with high ductility*.

ω phase strengthened 1.2GPa metastable β titanium alloy with high ductility

Junheng Gao[a]*, Alexander J Knowles[b], Dikai Guan[a], W. Mark Rainforth[a,*]

a Department of Materials Science and Engineering, The University of Sheffield, S1 3JD, UK

b Department of Materials, Royal School of Mines, Imperial College, London, SW7 2AZ, UK

*Corresponding author. E-mail address: junheng.gao@sheffield.ac.uk, m.rainforth@sheffield.ac.uk

Abstract

This paper provides a novel approach for exploiting ω phase strengthening in a metastable β titanium alloy whilst retaining high ductility. The addition of 1wt% Fe into our previously designed Ti-7Mo-3Cr alloy can efficiently control the growth of ω phase following air-cooling, resulting in a ultrahigh yield strength ($R_{p0.2}$ of 1210 MPa) with large ductility (ε_f of 0.15). Transmission electron microscopy of the annealed Ti-7Mo-3Cr-1Fe alloy revealed that the air-cooled Ti-7Mo-3Cr-1Fe exhibited extensive ω precipitates 1-9nm in size, which were larger than that of its water-quenched counterpart (0.5-4 nm). EBSD and TEM results of deformed alloys showed that the growth of ω phase in the air-cooled Ti-7Mo-3Cr-1Fe alloy modified the deformation mechanism from {332} twinning and dislocation slip, in the water-quenched alloy, to localized dislocation plasticity in ω-void channels.

Keywords: Metastable beta titanium alloy; ω phase; Strengthening; Yield strength

Metastable β titanium alloys with twinning and/or martensite transformation induced plasticity (TWIP and/or TRIP) have been exploited as biomedical and structural materials owing to their low elastic modulus, low biotoxicity, high strength and large uniform elongation [1-5]. Recently, promising mechanical properties (e.g. high ductility and high hardening rate) have been achieved in metastable β titanium alloys, such as Ti-12Mo[6], Ti-9Mo-6W[7, 8], Ti-10Cr[9] and Ti-7Mo-3Cr[10], with TRIP and/or TWIP effects (hereafter all the compositions are in mass %). However, the low yield strength (200 -500MPa) of these metastable β titanium alloys with TRIP and/or TWIP has been their "Achilles's heel", hindering their technological application. Although some metastable titanium alloys with high yield strength have been observed, such as gum metal [11], these alloys generally show a low work hardening rate and poor uniform elongation.

Depending on the chemical compositions and cooling rate, after solid solution heat treatment in the high temperature β phase region[3], the martensite transformation and secondary phase precipitation (e.g. alpha phase and ω phase) can be activated separately or simultaneously, or the single-phase bcc structure retained. These different microstructures strongly influence the deformation mechanisms that occur upon loading. In the recent past, the influence of the ω phase on the strengthening effect in metastable β titanium alloys has been the subject of considerable interest. For example, Liu et al. developed a series of spinal-support metastable β titanium alloys with changeable modulus via deformation induced ω transformation [9, 12]. Moreover, Sun et al. [13] proposed that low-temperature flash aging of a Ti-12Mo alloy can effectively enhance the yield strength while preserving substantial elongation-to-failure, where the ω embrittlement effect was successfully avoided by the accurate temperature and time control for supressing of ω growth and elemental partitioning. Lai et al.[14] also studied the effect ω phase formation on the deformation mechanism of a metastable Ti-Nb-Ta-Zr alloy, and they reported that the formation of ω phase enhanced the yield strength and shifted the deformation mechanisms from {332} twinning and martensite transformation, which were the main deformation mechanisms in the ω-free counterpart, to localized dislocation plasticity in ω-devoid channels.

In the current work, considering the formation of ω phase is also dependent on β phase stability (i.e. the amount of β stabilizers present) and cooling rate, we proposed a new route to exploit the ω phase strengthening effect while preserving high ductility. This led to a new metastable β titanium alloy, Ti-7Mo-3Cr-1Fe, optimised through β phase stability and cooling rate control. The Ti-7Mo-3Cr-1Fe alloy was developed based on our previously developed Ti-7Mo-3Cr alloy that had an initial deformation mechanisms of {332} and as {112} twinning and dislocation slip in water-quenched condition[10].

The Ti-7Mo-3Cr and Ti-7Mo-3Cr-1Fe alloys were arc melted from pure elements in a high-purity argon atmosphere. The ingots were homogenized at 1200°C for 3h under flowing argon and water quenched. It was then cold rolled from 6 to 2.4mm thickness and annealed at 850°C for 20 min under flowing argon, followed by water quenching or air cooling. X-ray diffraction was performed on a Siemens D5000 diffractometer fitted with a CuKα radiation source, at a scan rate of 0.1°/min and a step size of 0.01°. Tensile samples with a gauge dimension of 3mm×12.5mm×1.5mm were cut along the rolling direction and polished from the plate after heat treatment. Tensile tests were performed on a Zwick/Roell Z050 with laser extensometer at a strain rate of $4.0×10^{-4}$ s^{-1}. The annealed and tensile tested plate samples with 2.4mm

thickness were ground to ~100μm in thickness and punched to 3mm-diameter discs. Samples for EBSD imaging and TEM analysis were produced by twin-jet electropolished with a solution of 5% perchloric acid, 35% 2-butyoxyethanol and 60% methanol at -35℃. In order to obtain a relatively flat region at magnification of 500× for EBSD mapping, the samples were electropolished for a short time (30-40 seconds) to remove the residual deformation surface layer induced by mechanical polishing. EBSD was performed using a field emission gun scanning electron microscope (FEI Inspect F50 FEG SEM) operated at 20kV with a step size of 1μm for grain size analysis and 0.15μm for twinning and phase analysis. A Tecnai T20 transmission electron microscope (TEM) operated at 200 kV was used to characterize the annealed and deformed samples. A double aberration corrected microscope JEM-Z3100F-R005 operated at 300 kV was also used to characterize the air-cooled Ti-7Mo-3Cr-1Fe alloy. A high-angle annular dark-field scanning transmission electron microscopy (HAADF-STEM) (JEOL 2100F) coupled with energy-dispersive spectroscopy (Oxford Instruments EDX detector) was used to investigate possible elemental partitioning with 0.7nm spot size and 15° tilt toward EDX detector.

After annealing at 850℃ for 20 min, a fully recrystallized microstructure with a broad grain size distribution (maximum 205μm, minimum 7μm) was observed for air-cooled Ti-7Mo-3Cr-1Fe alloy, Supplementary Figure 1, which corresponds well with the grain size distribution of Ti-7Mo-3Cr alloy[10]. The EBSD map indicated a single phase microstructure free from annealing twins and second phases for both air-cooled and water-quenched alloys.

Supplementary Figure 2 shows the XRD profiles of Ti-7Mo-3Cr-1Fe and Ti-7Mo-3Cr alloys subjected to air cooling or water quenching after annealing at 850℃ for 20 mins. For the water-quenched Ti-7Mo-3Cr-1Fe alloy, only peaks corresponding to β phase were identified, while both β phase and ω phase were observed in the air-cooled Ti-7Mo-3Cr-1Fe alloy, suggesting that the slower cooling rate induced more ω phase formation. For Ti-7Mo-3Cr alloy, β and ω phases were observed in the both air-cooled and water-quenched alloys. This suggests that both cooling conditions and the addition of 1% Fe can tailor the formation of ω phase.

Fig.1a shows a dark-field (DF) micrograph of the air-cooled alloy recorded using $(\bar{1}010)_{\omega 1}$, which shows the extensive formation of ω precipitates with a size in range of 1 to 9nm. The inset in Fig.1a presents the selected-area electron diffraction (SAED) pattern recorded along $[011]_{\beta}$ zone axis. Besides the distinct reflections from the β matrix, the pronounced diffraction intensity maxima at 1/3 and 2/3 $\{011\}_{\beta}$ positions provide further evidence of the extensive

formation of ω precipitates. The DF image of the water-quenched alloy in Fig.1b also shows the extensive formation of ω precipitates, but the size of these precipitates was much smaller, 0.5 to 4nm, than that of air-cooled alloy. This was in agreement with the SAED pattern in the inset of Fig.1b, where the diffraction intensity maxima corresponding to ω phase were much weaker than that of ω phase in air-cooled alloy, suggesting that of amount of ω phase is smaller than that of air-cooled alloy. The DF micrographs of air-cooled and water-quenched Ti-7Mo-3Cr alloys are shown in Figs.1c and d. Insets in Figs.1c and d are their corresponding SAED patterns. In comparison with air-cooled and water-quenched Ti-7Mo-3Cr-1Fe alloys, the corresponding air-cooled and water-quenched Ti-7Mo-3Cr alloys exhibit larger ω precipitates, suggesting the addition of 1% Fe can tailor the ω precipitates size, instead of rapid growth of ω precipitates observed in air-cooled Ti-7Mo-3Cr alloy.

The ω phase in the air-cooled alloy was further characterized using HRTEM. Fig.2a shows the HRTEM image recorded along the $[\bar{1}10]_\beta$ zone axis, confirming the extensive formation of ω phase. Fig.2b shows the fast Fourier transform (FFT) pattern where both the β-associated and ω-associated spots are observed, which are consistent with the SAED pattern in Fig.1b. The inverse FFT image obtained by masking the ω spots (blue circles in Fig.2b) is shown in Fig.2c. Two ω variants are observed in the inverse FFT image, termed as ω_1 and ω_2. The size of ω_1 in the major and minor axis is 4.8nm and 4.1nm, respectively, while the size of ω_2 in the major and minor axis is 4.9nm and 3.8nm, which are consist with Fig.1a.

The STEM-HAADF image and corresponding EDX composition maps (Supplementary Figure 3) show no evidence of composition variation correlated with ω in the air-cooled Ti-7Mo-3Cr-1Fe alloy. The EDX maps show a uniform K-shell X-ray intensity for Ti, Mo, Cr and Fe over the entire mapping area, which is consist with the EDX composition maps of Ti-Nb alloy[15].

Fig.3 presents the tensile stress-strain curves of the Ti-7Mo-3Cr-1Fe alloy subjected to air-cooling or water-quenching after annealing at 850℃ for 20 min. For comparison, the stress-strain curves of air-cooled and water-quenched Ti-7Mo-3Cr alloys are also shown. The water-quenched Ti-7Mo-3Cr-1Fe exhibits a yield strength, $R_{p0.2}$ of 648MPa, ultimate tensile strength of 924MPa and strain to fracture of 0.25. Interestingly, air cooling substantially enhanced the yield strength ($R_{p0.2}$ of 1210MPa) and ultimate tensile strength (1245MPa) of the Ti-7Mo-3Cr-1Fe alloy, while retaining a large strain to fracture of 0.15. Although the Ti-7Mo-3Cr alloy exhibited high strength and high ductility in the water-quenched condition[10], the air-cooled Ti-7Mo-3Cr alloy fractured without observable plasticity.

Supplementary Figure 4a shows that neither martensite transformation nor twinning was observed in the air-cooled alloy at 3% tensile strain, although several band structures (marked by white arrows in Supplementary Figure 4a) were occasionally observed within some grains. For the water-quenched alloy (Supplementary Figure 4b), extensive {332}⟨113⟩ twins were observed, especially in relative large grains, where 2 or 3 twin variants activated. This corresponded well with our previous work in Ti-7Mo-3Cr alloy where the activation of twins was governed by both Schmid factor and grain size[10].

In order to determine the initial deformation mechanism, TEM analysis was conducted on the air-cooled Ti-7Mo-3Cr-1Fe after 3% total strain (Fig.4). The BF image in Fig.4a shows that a high density of nano-band structures are observed. According to the β[110] zone axis SAED pattern in Fig.4b, only β phase and ω phase are observed, indicating that these nano-band structures are not deformation twins or stress induced martensite. In order to identify these nano-band structures, DF images (Figs.4c and d) were obtained using ω reflections marked by ω_1 and ω_2 in Fig.4b. The DF images (Figs.4c and d) show that these nano-band structures are poor in ω phase, suggesting that these nano-band structures are ω-devoid dislocation channels, as reported in a furnace-cooled Ti-Nb alloy[14].

It is well accepted that the isothermal ω phase can cause embrittlement in metastable β titanium alloys. The growth of ω phase leads a rapid increase of local elastic strains around the interface between ω phase and β matrix, which act as obstacles for gliding dislocations[13]. The gliding dislocations are believed to cut through ω phase on the $\{112\}_\beta//\{\bar{1}100\}_\omega$ planes[14]. The growth of ω phase increases the critical resolved shear stress for dislocation motion, resulting in a high yield strength and loss of ductility (embrittlement). In order to exploit the strengthening effect of ω phase without significant loss of ductility, restricting the rapid ω phase growth is necessary.

The growth of ω phase in β titanium alloys is dependent on β stability (i.e. amount of β stabilizers) and cooling rate [1, 4, 14]. According to experimental knowledge and simulation work[1], Fe is one of the strongest β stabilizers among transition metals. The addition of Fe can greatly decreases the formation energy of β phase and meanwhile, Fe only has very limited effect on the formation energy of ω phase, so Fe is also one of the most efficient elements suppressing ω phase formation among the transition metals [1]. In the water-quenched Ti-Fe-Mo alloy [16, 17], very limited incommensurate ω phase (1nm domains) was observed. The different mechanical behaviour between the air-cooled Ti-7Mo-3Cr and Ti-7Mo-3Cr-1Fe

alloys in Fig.3 and microstructural analysis in Figs.1 and 2 confirmed that the addition of 1wt% Fe successfully tailored the ω precipitates size in the air-cooled Ti-7Mo-3Cr-1Fe alloy, leading to a superior combination of high strength and high ductility.

Mantri et al. reported that, after annealing at 475 °C for 48h, the partitioning of Mo induced by the precipitation of ω phase in Ti-12Mo significantly stabilized the β matrix, resulting in a change of deformation mechanism from TWIP and TRIP to dislocation slip[18]. In this work, the change in the deformation mechanism in the air-cooled Ti-7Mo-3Cr-1Fe alloy was attributed to the growth of ω phase that acts as a strong barrier for $\{1\bar{1}0\}_\beta\langle110\rangle_\beta$ atomic movements[14]. In metastable β titanium alloys, the shuffling of $\{1\bar{1}0\}_\beta$ planes along the $\langle110\rangle_\beta$ direction is involved in the martensite transformation and twinning [14, 19]. In order to determine the effect of ω phase on the suppression of martensite transformation and twinning, Lai et al. calculated the shear modulus along $\{11\bar{2}0\}_\omega$ as this is parallel to $\{1\bar{1}0\}_\beta$ [14]. The shear modulus along $\{11\bar{2}0\}_\omega$ was calculated to be 39.55GPa, which was much larger than that of $\{1\bar{1}0\}_\beta$, <18GPa[14]. Therefore, it was the formation of a high density of larger ω precipitates in air-cooled Ti-7Mo-3Cr-1Fe alloy that acted as strong local barriers to $\{1\bar{1}0\}_\beta\langle110\rangle_\beta$ atomic movements, which completely suppressed $\{332\}\langle113\rangle$ twinning. As deformation twinning was completely suppressed in the air-cooled Ti-7Mo-3Cr-1Fe alloy, the plastic deformation of this alloy relied on localized dislocation slip in the nano-sized ω-devoid dislocation channels (Fig.4). The formation of the ω-devoid dislocation channels is attributed to the gliding of dislocations on the $\{112\}_\beta$ slip plane cutting though ω precipitates via the prismatic slip plane $\{\bar{1}100\}_\omega$ of the ω phase, which is parallel to the $\{112\}_\beta$ slip plane, and so promoted transformation of ω to β [20].

In summary, we report a new route to exploit the ω phase strengthening to obtain a superior combination of strength and ductility in a Ti-7Mo-3Cr-1Fe beta titanium alloy. The addition of 1wt% Fe in Ti-7Mo-3Cr alloy efficiently controlled the rapid growth of ω phase in the air-cooled condition, leading to an ultra-high yielding strength ($R_{p0.2}$ of 1210MPa) and large strain to failure (15%). We believe that much more substantial improvements can be achieved by further composition and cooling rate optimization.

Acknowledgements

References

[1] L.F. Huang, B. Grabowski, J. Zhang, M.-J. Lai, C.C. Tasan, S. Sandlöbes, D. Raabe, J. Neugebauer, Acta Materialia, 113 (2016) 311-319.

[2] M. Niinomi, M. Nakai, J. Hieda, Acta Biomaterialia, 8 (2012) 3888-3903.

[3] M. Abdel-Hady, K. Hinoshita, M. Morinaga, Scripta Materialia, 55 (2006) 477-480.

[4] P. Wang, M. Todai, T. Nakano, Journal of Alloys and Compounds, 766 (2018) 511-516.

[5] P. Wang, Y. Feng, F. Liu, L. Wu, S. Guan, Materials Science and Engineering: C, 51 (2015) 148-152.

[6] F. Sun, J.Y. Zhang, M. Marteleur, T. Gloriant, P. Vermaut, D. Laillé, P. Castany, C. Curfs, P.J. Jacques, F. Prima, Acta Materialia, 61 (2013) 6406-6417.

[7] F. Sun, J.Y. Zhang, M. Marteleur, C. Brozek, E.F. Rauch, M. Veron, P. Vermaut, P.J. Jacques, F. Prima, Scripta Materialia, 94 (2015) 17-20.

[8] J. Gao, J. Nutter, X. Liu, D. Guan, Y. Huang, D. Dye, W.M. Rainforth, Scientific Reports, 8 (2018) 7512.

[9] H. Liu, M. Niinomi, M. Nakai, J. Hieda, K. Cho, Scripta Materialia, 82 (2014) 29-32.

[10] J. Gao, Y. Huang, D. Guan, A.J. Knowles, L. Ma, D. Dye, W.M. Rainforth, Acta Materialia, 152 (2018) 301-314.

[11] T. Saito, T. Furuta, J.-H. Hwang, S. Kuramoto, K. Nishino, N. Suzuki, R. Chen, A. Yamada, K. Ito, Y. Seno, T. Nonaka, H. Ikehata, N. Nagasako, C. Iwamoto, Y. Ikuhara, T. Sakuma, Science, 300 (2003) 464-467.

[12] H. Liu, M. Niinomi, M. Nakai, K. Cho, Acta Biomaterialia, 24 (2015) 361-369.

[13] F. Sun, J.Y. Zhang, P. Vermaut, D. Choudhuri, T. Alam, S.A. Mantri, P. Svec, T. Gloriant, P.J. Jacques, R. Banerjee, F. Prima, Materials Research Letters, 5 (2017) 547-553.

[14] M.J. Lai, T. Li, D. Raabe, Acta Materialia, 151 (2018) 67-77.

[15] E.L. Pang, E.J. Pickering, S.I. Baik, D.N. Seidman, N.G. Jones, Acta Materialia, 153 (2018) 62-70.

[16] A.J. Knowles, N.G. Jones, O.M.D.M. Messé, J.S. Barnard, C.N. Jones, H.J. Stone, International Journal of Refractory Metals and Hard Materials, 60 (2016) 160-168.

[17] A.J. Knowles, T.-S. Jun, A. Bhowmik, N.G. Jones, T.B. Britton, F. Giuliani, H.J. Stone, D. Dye, Scripta Materialia, 140 (2017) 71-75.

[18] S.A. Mantri, D. Choudhuri, T. Alam, V. Ageh, F. Sun, F. Prima, R. Banerjee, Scripta Materialia, 130 (2017) 69-73.

[19] H.Y. Kim, L. Wei, S. Kobayashi, M. Tahara, S. Miyazaki, Acta Materialia, 61 (2013) 4874-4886.

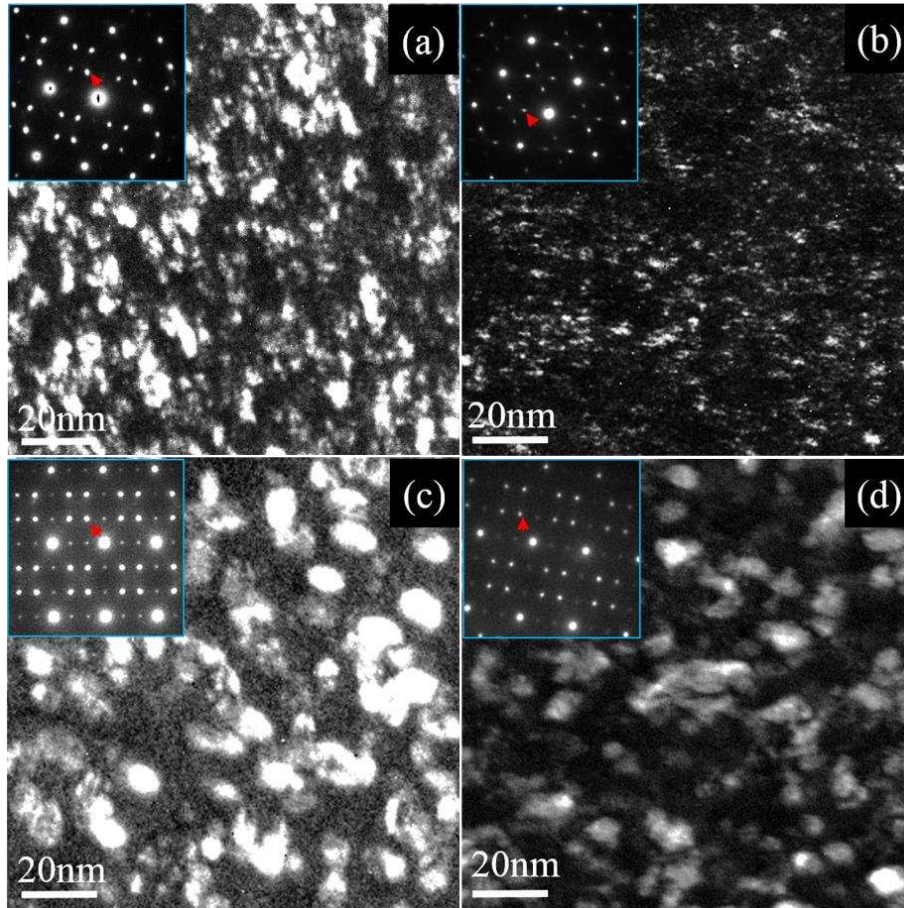[20] M.J. Lai, C.C. Tasan, D. Raabe, Acta Materialia, 100 (2015) 290-300.

Fig. 1. TEM analysis of the annealed Ti-7Mo-3Cr-1Fe and Ti-7Mo-3Cr alloys subjected to air cooling or water quenching. (a) and (b) DF micrographs of Ti-7Mo-3Cr-1Fe alloy subjected to air cooling and water quenching respectively; (c) and (d) DF micrographs of Ti-7Mo-3Cr alloy subjected to air cooling and water quenching respectively. DF images were recorded using $(\bar{1}010)_{\omega1}$, marked by red arrow in the SAED patterns (Insets). SAED patterns were recorded with beam//$[011]_{\beta}$.
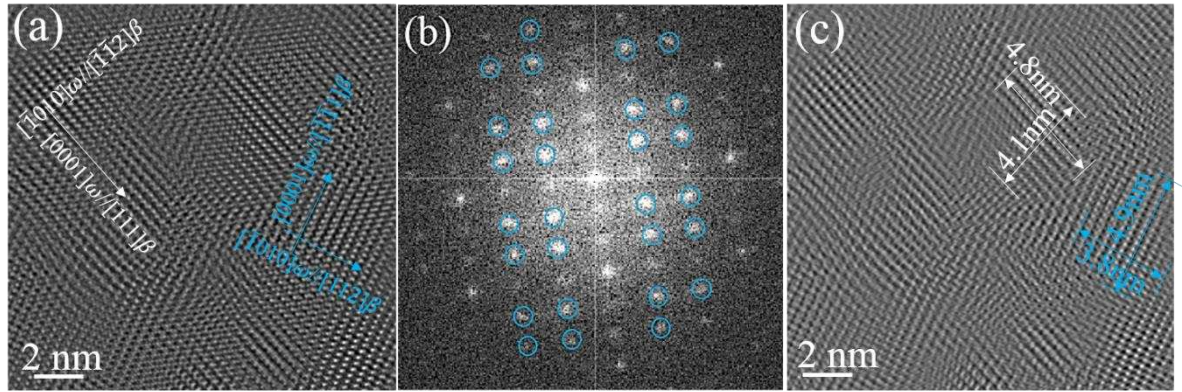
Fig.2.HRTEM study of the annealed Ti-7Mo-3Cr-1Fe alloy subjected to air cooling. (a) HRTEM image recorded along the $[\bar{1}10]_\beta$ zone axis,(b) corresponding FFT pattern, (c) inverse FFT image by masking the ω spots (blue circles) in (b).
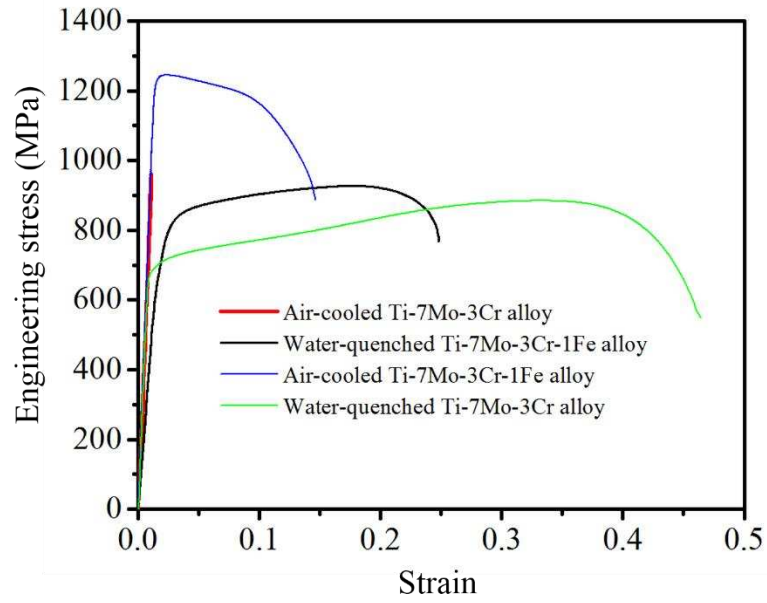
Fig.3. Tensile engineering stress-strain tensile curves of Ti-7Mo-3Cr and Ti-7Mo-3Cr-1Fe alloys subjected to air cooling or water quenching after annealing.
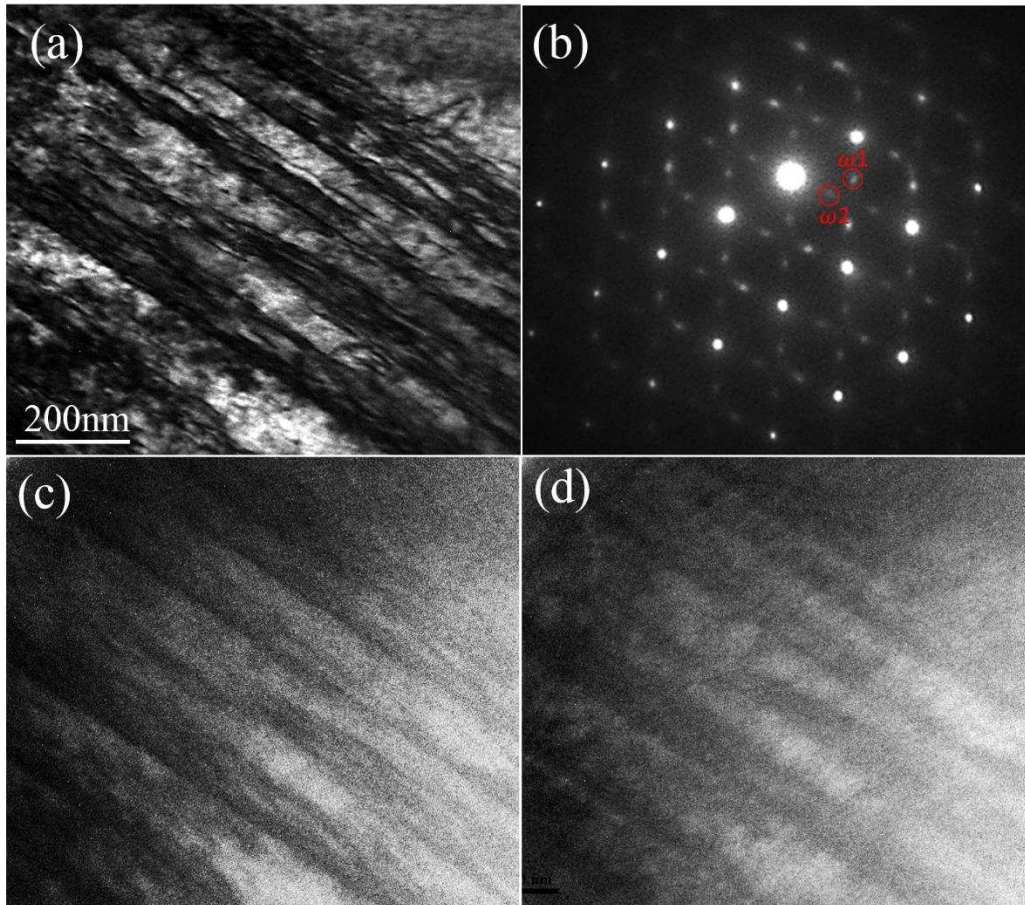
Fig.4. TEM analysis of the tensile-tested air-cooled Ti-7Mo-3Cr-1Fe alloy after 3% total strain. (a) BF image and its indexed β[110] zone axis SAED pattern (b). (c) and (d) corresponding DF images acquired using ω reflections marked by ω_1(c) and ω_2 (d) in (b).